UC Davis
UC Davis Previously Published Works

Title
DETECTION OF LYMAN-ALPHA EMISSION FROM A TRIPLY IMAGED z = 6.85 GALAXY BEHIND MACS J2129.4−0741

Permalink

Journal

ISSN

Authors
Huang, Kuang-Han
Lemaux, Brian C
Schmidt, Kasper B
et al.

Publication Date
2016-05-20

DOI

Peer reviewed

DETECTION OF LYMAN-ALPHA EMISSION FROM A TRIPLY-IMAGED $z = 6.85$ GALAXY BEHIND MACS J2129.4−0741

Kuang-Han Huang[1], Brian C. Lemaux[1], Kasper B. Schmidt[2], Austin Hoag[1], Maruša Bradač[1], Tommaso Treu[3], Mark Dijkstra[4], Adriano Fontana[5], Alaina Henry[6], Matthew Malkan[3], Charlotte Mason[3], Takahiro Morishita[3,7], Laura Pentericci[5], Russell E. Ryan, Jr.[8], Michele Trenti[9], and Xin Wang[3]

Draft version November 13, 2018

ABSTRACT

We report the detection of Lyα emission at $\sim$ 9538Å in the Keck/DEIMOS and *HST* WFC3 G102 grism data from a triply-imaged galaxy at $z = 6.846 \pm 0.001$ behind galaxy cluster MACS J2129.4−0741. Combining the emission line wavelength with broadband photometry, line ratio upper limits, and lens modeling, we rule out the scenario that this emission line is [O II] at $z = 1.57$. After accounting for magnification, we calculate the weighted average of the intrinsic Lyα luminosity to be $\sim 1.3 \times 10^{42}$ erg s^{-1} and Lyα equivalent width to be 74 ± 15Å. Its intrinsic UV absolute magnitude at 1600Å is -18.6 ± 0.2 mag and stellar mass $(1.5 \pm 0.3) \times 10^7$ $M_\odot$, making it one of the faintest (intrinsic $L_{\rm UV} \sim 0.14$ $L_{\rm UV}^*$) galaxies with Lyα detection at $z \sim 7$ to date. Its stellar mass is in the typical range for the galaxies thought to dominate the reionization photon budget at $z \gtrsim 7$; the inferred Lyα escape fraction is high ($\gtrsim 10\%$), which could be common for sub-L^* $z \gtrsim 7$ galaxies with Lyα emission. This galaxy offers a glimpse of the galaxy population that is thought to drive reionization, and it shows that gravitational lensing is an important avenue to probe the sub-L^* galaxy population.

Subject headings: galaxies: evolution — galaxies: high-redshift — methods: data analysis — gravitational lensing: strong

1. INTRODUCTION

Galaxy cluster fields have become popular survey fields for the high-redshift universe, because strong gravitational lensing boosts the number counts in the bright end of the UV luminosity function (LF) and probes fainter intrinsic luminosities than in blank fields (e.g., Coe et al. 2015). Intrinsically fainter galaxies at $z \gtrsim 3$ are also more likely to exihibit Lyα in emission, a result of correlation between UV luminosity and dust attenuation (e.g., Schaerer et al. 2011). To constrain the properties of background galaxies, one needs a precise lensing map of the galaxy cluster, constructed using the positions and redshifts of multiply-imaged background galaxies (e.g., Bradač et al. 2009); in particular, when a background galaxy has multiple images, their positions can be used to constrain the galaxy's redshift.

Several multiply-imaged $z \geq 6$ galaxies have been discovered previously. Some have their redshifts confirmed by spectroscopy through the detection of their Lyα emission (e.g., Richard et al. 2011; Balestra et al. 2013; Vanzella et al. 2014), while others are not confirmed by spectroscopy but have strong constraints from both photometry and lensing to be at redshifts up to $\sim$ 11 (e.g., Zitrin et al. 2014, and references therein). For the latter group of objects, gravitational lensing gives credence to the high-redshift interpretation even when no spectral features are detected, something that is not available in blank fields.

Here we report the detection of Lyα emission, by both Keck/DEIMOS and *HST* WFC3/IR grism, from three sources lensed by the galaxy cluster MACS J2129.4−0741 (hereafter MACS2129; Ebeling et al. 2007) — the highest-redshift multiply-imaged system spectroscopically confirmed to date. Two of the three sources (Images A and B) are selected as Lyman Break Galaxies (LBGs) at $z \sim 6 - 7$ by Bradley et al. (2014), and all three sources are considered multiple images of the same galaxy at $z = 6.5$ in Zitrin et al. (2015). Based on their photometric, spectroscopic, and lensing constraints, the most natural explanation is that they are multiple images of the same galaxy at $z = 6.85$. We discuss the photometry in Section 2, the spectroscopy in Section 3, the lens modeling in Section 4, and their physical properties and implications for reionization in Section 5. We adopt the cosmological parameters $H_0 = 70$ km s^{-1} Mpc^{-1}, $\Omega_m = 0.3$, and $\Omega_\Lambda = 0.7$ in our analyses, and all magnitudes are in the AB system.

2. PHOTOMETRIC CONSTRAINTS

We use deep *HST* and *Spitzer* imaging data for MACS2129 to derive photometric constraints for the three images. The *HST* imaging data were taken as a part of the Cluster Lensing And Supernova survey with Hubble (CLASH; Postman et al. 2012) program. We perform photometry in the same way as Huang et al.

E-mail: khhuang@ucdavis.edu

[1] University of California Davis, 1 Shields Avenue, Davis, CA 95616, USA; khhuang@ucdavis.edu
[2] Leibniz-Institut für Astrophysik Potsdam (AIP), An der Sternwarte 16, 14482, Potsdam, Germany
[3] Department of Physics and Astronomy, UCLA, Los Angeles, CA 90095, USA
[4] Institute of Theoretical Astrophysics, University of Oslo, P.O. Box 1029, NO-0315 Oslo, Norway
[5] INAF Osservatorio Astronomico di Roma, Via Frascati 33,00040 Monteporzio (RM), Italy
[6] Astrophysics Science Division, Goddard Space Flight Center, Code 665, Greenbelt, MD 20771, USA
[7] Astronomical Institute, Tohoku University, Aramaki, Aoba, Sendai 980-8578, Japan
[8] Space Telescope Science Institute, Baltimore, MD 21218, USA
[9] School of Physics, The University of Melbourne, VIC 3010, Australia

TABLE 1
SUMMARY OF MULTIPLE IMAGES[a]

		Image A	Image B	Image C
R.A.	(deg.)	322.350936	322.353239	322.353943
Decl.	(deg.)	-7.693322	-7.697442	-7.681646
$\mu_{\rm best}$		$11.0^{+0.1}_{-0.7}$	$5.4^{+0.1}_{-0.1}$	$2.6^{+0.1}_{-0.1}$
F225W	(mag)	> 26.30	> 27.07	> 27.77
F275W	(mag)	> 26.57	> 27.16	> 27.90
F336W	(mag)	> 26.75	> 27.51	> 28.21
F390W	(mag)	$\cdots$	> 28.00	> 28.65
F435W	(mag)	26.70 ± 0.63	> 27.81	> 28.27
F475W	(mag)	> 27.53	> 28.17	> 28.79
F555W	(mag)	27.64 ± 0.71	> 28.58	> 29.25
F606W	(mag)	> 27.76	> 28.39	> 28.73
F625W	(mag)	26.64 ± 0.69	> 27.99	28.46 ± 0.89
F775W	(mag)	> 27.23	27.89	> 28.48
F814W	(mag)	27.07 ± 0.52	28.76 ± 0.99	> 29.45
F850LP	(mag)	$(25.69 \pm 0.35)^{\rm b}$	> 27.58	> 28.08
F105W	(mag)	25.77 ± 0.30	26.33 ± 0.21	27.58 ± 0.34
F110W	(mag)	25.33 ± 0.17	26.42 ± 0.23	27.84 ± 0.41
F125W	(mag)	25.70 ± 0.20	26.42 ± 0.21	27.42 ± 0.28
F140W	(mag)	25.62 ± 0.17	26.63 ± 0.24	28.26 ± 0.47
F160W	(mag)	25.83 ± 0.23	26.64 ± 0.21	28.13 ± 0.54
[3.6]	(mag)	> 24.15	26.19 ± 0.51	> 27.12
[4.5]	(mag)	> 25.22	> 26.57	> 27.09
$M_{\rm UV} - 2.5\log(\mu/\mu_{\rm best})$	(mag)	-18.6 ± 0.2	-18.6 ± 0.2	-18.4 ± 0.3
$M_* \times \mu/\mu_{\rm best}$	$(10^7\ M_\odot)$	$1.7^{+0.6}_{-0.2}$	$1.6^{+1.0}_{-0.04}$	$1.3^{+0.3}_{-0.4}$
SFR $\times \mu/\mu_{\rm best}$	$(M_\odot\,{\rm yr}^{-1})$	$1.8^{+0.3}_{-0.3}$	$1.7^{+0.9}_{-0.3}$	$0.8^{+0.2}_{-0.1}$
sSFR	$({\rm Gyr}^{-1})$	$105.1^{+0.0}_{-42.1}$	$105.1^{+0.0}_{-42.1}$	$65.7^{+39.4}_{-10.3}$
Age	(Myr)	≤ 17	≤ 17	17^{+3}_{-7}
$E(B-V)^{\rm c}$	(mag)	< 0.05	< 0.05	< 0.05
$R_e \times \sqrt{\mu/\mu_{\rm best}}^{\rm d}$	(kpc)	0.8 ± 0.3	0.5 ± 0.1	0.4 ± 0.1
$\beta^{\rm e}$		$-2.49^{+1.39}_{-1.43}$	$-2.96^{+1.35}_{-1.68}$	≤ -1.89
$\chi^2_{z=6.85}$		6.5	5.1	1.4
$\chi^2_{z=1.57}$		9.4	22.1	5.0
Keck DEIMOS Measurement				
$t_{\rm exp}$	(ks)	21.6	40.2	40.2
$f_{\rm Ly\alpha}^{\rm DEIMOS}$	$(10^{-17}\ {\rm erg\,s^{-1}\,cm^{-2}})$	2.0 ± 0.1	1.1 ± 0.1	0.7 ± 0.1
$L_{\rm Ly\alpha}^{\rm DEIMOS} \times \mu/\mu_{\rm best}$	$(10^{42}\ {\rm erg\,s^{-1}})$	1.0 ± 0.1	1.2 ± 0.1	2.0 ± 0.3
$W_{\rm Ly\alpha}^{\rm DEIMOS}$	(Å)	60 ± 11	47 ± 9	170 ± 77
$\mathrm{SFR}_{\rm Ly\alpha}^{\rm DEIMOS} \times \mu/\mu_{\rm best}$	$(M_\odot\,{\rm yr}^{-1})$	1.0 ± 0.1	1.1 ± 0.1	1.9 ± 0.3
HST Grism Measurement				
$f_{\rm Ly\alpha}^{\rm PA328}$	$(10^{-17}\ {\rm erg\,s^{-1}\,cm^{-2}})$	3.5 ± 0.8	2.7 ± 0.8	2.1 ± 0.8
$f_{\rm Ly\alpha}^{\rm PA050}$	$(10^{-17}\ {\rm erg\,s^{-1}\,cm^{-2}})$	1.7 ± 1.0	4.4 ± 1.0	2.6 ± 1.0
$W_{\rm Ly\alpha}^{\rm PA328}$	(Å)	93 ± 27	100 ± 33	399 ± 237
$W_{\rm Ly\alpha}^{\rm PA050}$	(Å)	43 ± 27	160 ± 45	513 ± 300
$W_{\rm CIV}^{\rm PA328}$	(Å)	≤ 24	≤ 39	≤ 105
$W_{\rm CIII]}^{\rm PA050}$	(Å)	≤ 27	≤ 43	≤ 115

[a] All error bars and limits are 1σ values, and the errors for magnification factors $\mu_{\rm best}$ are random errors only.
[b] The F850LP data for Image A has some spurious flux that led to a nominal 3.3σ detection, and we exclude it from our SED fitting procedure, although including it does not change our results significantly.
[c] All three images have best-fit $E(B-V) = 0$.
[d] Effective radii are measured in the stacked WFC3/IR images.
[e] The UV slope measured from the median-stacked HST images is $-2.76^{+1.23}_{-1.12}$.

(2016): source detection is done in the coadded CLASH WFC3/IR image using SExtractor, and colors are measured in isophotal apertures. We do not match the PSFs of different HST bands because convolving each band with a PSF-matching kernel introduces additional noise and degrades the signal-to-noise ratios. We run a simple check of our HST photometry by fitting photometric redshifts ($z_{\rm phot}$) to all sources with S/N$\geq$ 3 in at least three filters, and confirm that the $z_{\rm phot}$ distribu-tion peaks within $\Delta z = \pm 0.1$ of the cluster redshift, $z_{\rm Clus} = 0.570$ (Postman et al. 2012).

The Spitzer/IRAC imaging data in 3.6 and 4.5 μm are obtained from SURFS UP (Bradač et al. 2014) supplemented with shallower data from The IRAC Lensing Survey (PI: Egami). The IRAC images reach a total integration time of ~ 30 hours in each band within the HST field of view. We follow the same procedure as in Huang et al. (2016) for IRAC photometry: the HST positions
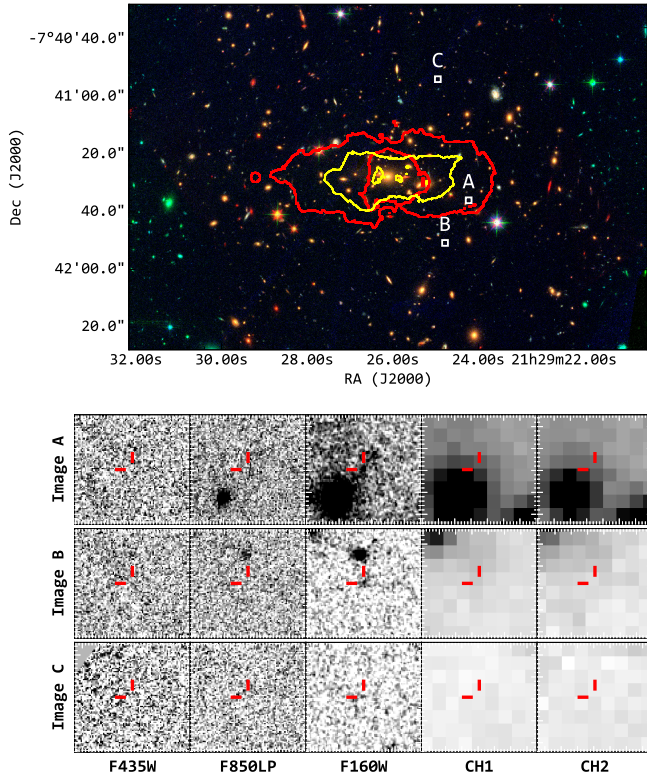
FIG. 1.— *Top:* RGB image covering the central $3' \times 2'$ of MACS2129.4−0741 and the locations of Images A, B, and C. The critical curve ($\mu = 100$) of the cluster at $z = 6.85$ ($z = 1.57$) is shown as red (yellow) lines. The $z = 1.57$ critical curve does not come close to reproducing the parity of the triple images. *Bottom:* Cutouts ($5''$ on each side) of all three images in F435W, F850LP, F160W, IRAC ch1, and IRAC ch2 (from left to right) are shown in each row. There is a nominal 3.3σ detection in the F850LP data for Image A that we consider spurious based on its morphology, and we exclude the F850LP magnitude of Image A in our analysis.

and morphologies are used as the high-resolution prior in the template-fitting code T-PHOT (Merlin et al. 2015), and IRAC PSFs are measured by stacking stellar objects found in both the main and flanking fields.

A summary of the photometric properties is listed in Table 1. We note that in the F850LP image, Image A has a nominal 3.3σ detection in the isophotal aperture that we think is likely spurious based on morphology. Therefore, we exclude the F850LP flux density of Image A in our analysis, although including it does not change our results significantly. Image A is also severely blended with its neighbor in the IRAC images, so we can only assign conservative upper limits to its IRAC flux densities. Both Images B and C are in relatively clean regions that are free from photometric foreground contamination, although neither has significant detections in the IRAC images.

3. SPECTROSCOPIC CONSTRAINTS

3.1. *Keck DEIMOS Data*

We targeted MACS2129 with Keck DEIMOS on 2014 September 01, 2015 May 15–16, and 2015 October 16 (all dates are UT). All the exposures were taken under generally photometric conditions, with seeing $\lesssim 1''$. The slit-masks with $1''$ wide slits were designed to include $z \gtrsim 7$ LBG candidates and, when slits were available, to also

include targets whose photometric redshifts had considerable probability at $z \geq 6$.

The stacked 2D and 1D spectra from all observing runs are shown in Figure 2. After stacking, we obtain significant line detections around 9538Å: before correcting for slit loss, the measured line fluxes for Images A, B, and C are $(9.9 \pm 0.6) \times 10^{-18}$, $(5.7 \pm 0.6) \times 10^{-18}$, and $(3.7 \pm 0.6) \times 10^{-18}$ erg s^{-1} cm^{-2}, respectively. Even for Image C, we achieve a 6.1σ detection from the stacked 1D spectrum. We account for a slit throughput of 0.8 for a source with half-light radius of $0''.3$ under $0''.8$ seeing (Lemaux et al. 2009) with additional corrections made for conditions and bulk astrometric offsets. The slit loss-corrected line fluxes and Lyα line luminosities are listed in Table 1.

We measure the Lyα equivalent widths (EWs) of each image using the F105W magnitudes to estimate the continuum level. The EWs of each image are reported in Table 1, and the weighted average EW (by S/N) is 74 ± 15Å. Because the S/N ratios are higher in DEIMOS data than in *HST* grism data (Section 3.2), we use the DEIMOS measurement as the fiducial values. The high EW, coupled with the blue rest-frame UV continuum slope $\beta = -2.76^{+1.23}_{-1.12}$ (measured from the stacked *HST* images of the three sources), implies a high Lyα escape fraction of $\gtrsim 10\%$ from local Lyα-emitting galaxies (Hayes et al. 2014; Henry et al. 2015). The Lyα escape fraction could also be crudely estimated by converting the Lyα luminosity into star formation rate (SFR) and compared with the UV-derived SFR. With this method, we estimate the Lyα escape fraction to be $\gtrsim 50\%$ assuming no dust correction for rest-frame UV flux.

We fit a truncated Gaussian profile to the stacked 1D spectrum of all images to estimate the line width and find the half width at half maximum (HWHM) on the red side of the line to be 145 ± 8 km s^{-1} (random error only, after accounting for an instrumental resolution of 1.93Å). The emission lines for Images A and B are individually broad enough to be resolved by the 1200G grating of DEIMOS, so we measure their line asymmetries $1/a_\lambda \equiv (\lambda_c - \lambda_{10,b})/(\lambda_{10,r} - \lambda_c)$, where λ_c is the central wavelength of the emission, and $\lambda_{10,r}$ ($\lambda_{10,b}$) is the wavelength where the flux first exceeds 10% of the peak redward (blueward) of the peak. The line asymmetries $1/a_\lambda$ for Images A and B are 0.35 and 0.71, consistent with the range of values for Lyα emission showing depressed blue wings. Therefore, the line shapes also support the Lyα interpretation.

3.2. *HST Grism Data*

HST WFC3/IR G102 and G141 grism data for MACS2129 were taken as part of the Grism Lens-Amplified Survey from Space (GLASS) program (Schmidt et al. 2014; Treu et al. 2015). GLASS obtained 10-orbit G102 data and 4-orbit G141 data for each cluster, aiming to probe the Lyα LF at $z \gtrsim 6$ and reaching uniform sensitivity across the two grisms that continuously cover 0.81μm – 1.69μm. For each cluster field, grism data were taken in two independent position angles (PAs; 50° and 328° for MACS2129) to facilitate contamination removal.

Schmidt et al. (2016) published the grism search on 159 LBGs from the first six clusters covered by GLASS,
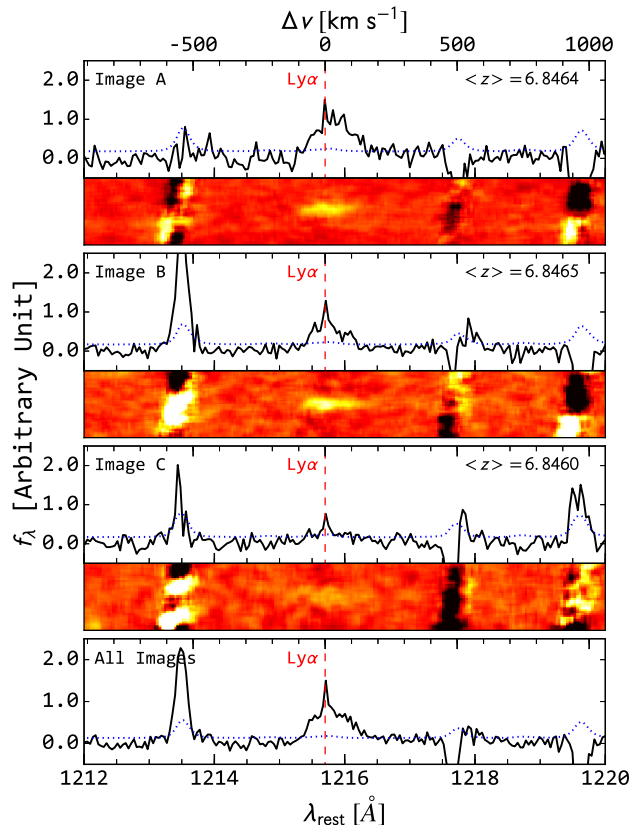
Fig. 2.— Full-depth 1D and 2D Keck/DEIMOS spectra for each image. In the 1D spectra panels, flux density is shown in solid lines, and RMS is shown in dotted lines. The rest-frame wavelength scale is shown on the bottom and the velocity scale is shown on top. The stacked 2D spectra are smoothed by a boxcar filter of width 5 pixels. Spectra are shifted slightly to align the peak wavelengths (shown by a vertical dashed line), and the Lyα redshifts determined by the peaks are indicated in the top-right corners.

including MACS2129. They showed that 24 out of 159 LBGs have emission line detections consistent with being Lyα, including Images B and C in this Letter; both sources have emission line detections around 9570 Å, corresponding to a Lyα redshift $z = 6.87$. However, due to the wavelength uncertainty of the grism spectra (~ 30 Å), the Lyα redshift cannot be determined to better than $\Delta z = 0.02$. We show the extracted grism spectra for all three images in Figure 3 and the measured Lyα fluxes in Table 1.

Image A is not in the $z \gtrsim 7$ LBG sample of Schmidt et al. (2016) because it was not selected as an LBG at $z \sim 6 - 7$ by multiple groups due to the spurious F850LP flux. But extraction of the grism spectra for Image A also shows an emission line at ~ 9570 Å ($\sim 4\sigma$ detection). This is observed in the PA $= 328°$ spectrum not affected by contamination, consistent with being Lyα emission at the same redshift as Images B and C.

Any (or all) of the three emission lines detected in grism spectra could also be the (unresolved) [O II] line at $z = 1.57$, but our Keck DEIMOS spectra do not show any signs of resolved [O II] doublets even though the spectral resolution is sufficient. Furthermore, the G141 grism data provide the wavelength coverage to detect (or rule out) [O III] emission lines at $z = 1.57$. We do not find significant detections at the expected [O III] wave-

length in the G141 spectra, and the 2σ upper limits for $f_{[OIII]}/f_{[OII]}$ range between 0.23 and 0.61, with a median $f_{[OIII]}/f_{[OII]} < 0.35$. At $z = 1.57$, this galaxy would have had a stellar mass of $\sim 2 \times 10^8$ $M_\odot$ and a sub-solar metallicity according to the mass-metallicity relation derived at $z \sim 2$, which implies $f_{[OIII]}/f_{[OII]} \geq 2$ (Henry et al. 2013). Therefore, we rule out the [O II] interpretation of the emission lines.

Other rest-frame UV nebular emission lines like C IV $\lambda1549$ and C III] $\lambda1909$ have been proposed as alternative features for redshift confirmation at $z \geq 6$ because they are not attenuated by the intergalactic medium (e.g., Stark et al. 2015a). Detections of C IV and C III] would also allow photoionization modeling to constrain the ionization parameter and metallicity (e.g. Erb et al. 2010). The GLASS G141 spectra cover the wavelengths of both C IV and C III] at $z = 6.85$, but we do not detect any C IV or C III] emission. The expected locations of C IV and C III] in the G141 spectra are marked by white circles in Figure 3, and we list the 1σ EW limits for C IV and C III] in Table 1. The most stringent limit on the rest-frame C IV and C III] EW is $\lesssim 25$Å (measured from Image A with $\mu = 11$), still not quite sufficient to detect the typical EWs of C IV and C III] emission (≤ 25Å) from low-metallicity galaxies (e.g., Stark et al. 2014; Rigby et al. 2015; Stark et al. 2015a,b). Schmidt et al. (2016) also derived a 2σ upper limit of C IV (C III]) to Lyα flux ratio of 0.32 (0.23) from a stack of eight $z \gtrsim 7$ Lyα-emitting galaxies. Therefore, detecting the C IV and C III] emission at $z \gtrsim 7$ is still quite challenging from the available HST grism spectra.

4. GRAVITATIONAL LENS MODELING

Gravitational lens modeling of MACS2129 is made difficult by the sparsity of known multiple image systems with spectroscopic redshifts. Zitrin et al. (2015) presented the first two lens models of the cluster using the CLASH photometry. While both models are constrained using 8 multiple image systems, only one of them (system 1 in Zitrin et al. 2015) was spectroscopically confirmed (see also Christensen et al. 2012). Moreover, system 1 is a rare example of a sextuply-imaged galaxy with a spectroscopic redshift $z = 1.364$; the unusual configuration and multiplicity of this system makes the modeling challenging, and neither model reproduces the multiplicity of system 1. The Zitrin et al. (2015) models do reproduce the positions of the $z = 6.85$ triple-image system accurately, but they predict that Image B is roughly twice as magnified as Image A, in disagreement with the observed ratio.

To improve the estimates of the absolute magnifications of the triply-imaged galaxy, we create a new lens model of MACS2129 using additional spectroscopic redshifts from GLASS and from CLASH-VLT (186.A-0798; PI: P. Rosati; Monna et al. in prep.). We identify a new $z = 1.04 \pm 0.01$ multiple-image system that is not identified by Zitrin et al. (2015), and while we have spectroscopic redshifts for parts of other multiple-image systems, we are not confident enough in any other system as a whole. To be conservative, we model the cluster using system 1, the aforementioned new system at $z = 1.04$, and the triply-imaged system at $z = 6.85$. We employ the lens modeling method SWUnited (Bradač et al. 2005,
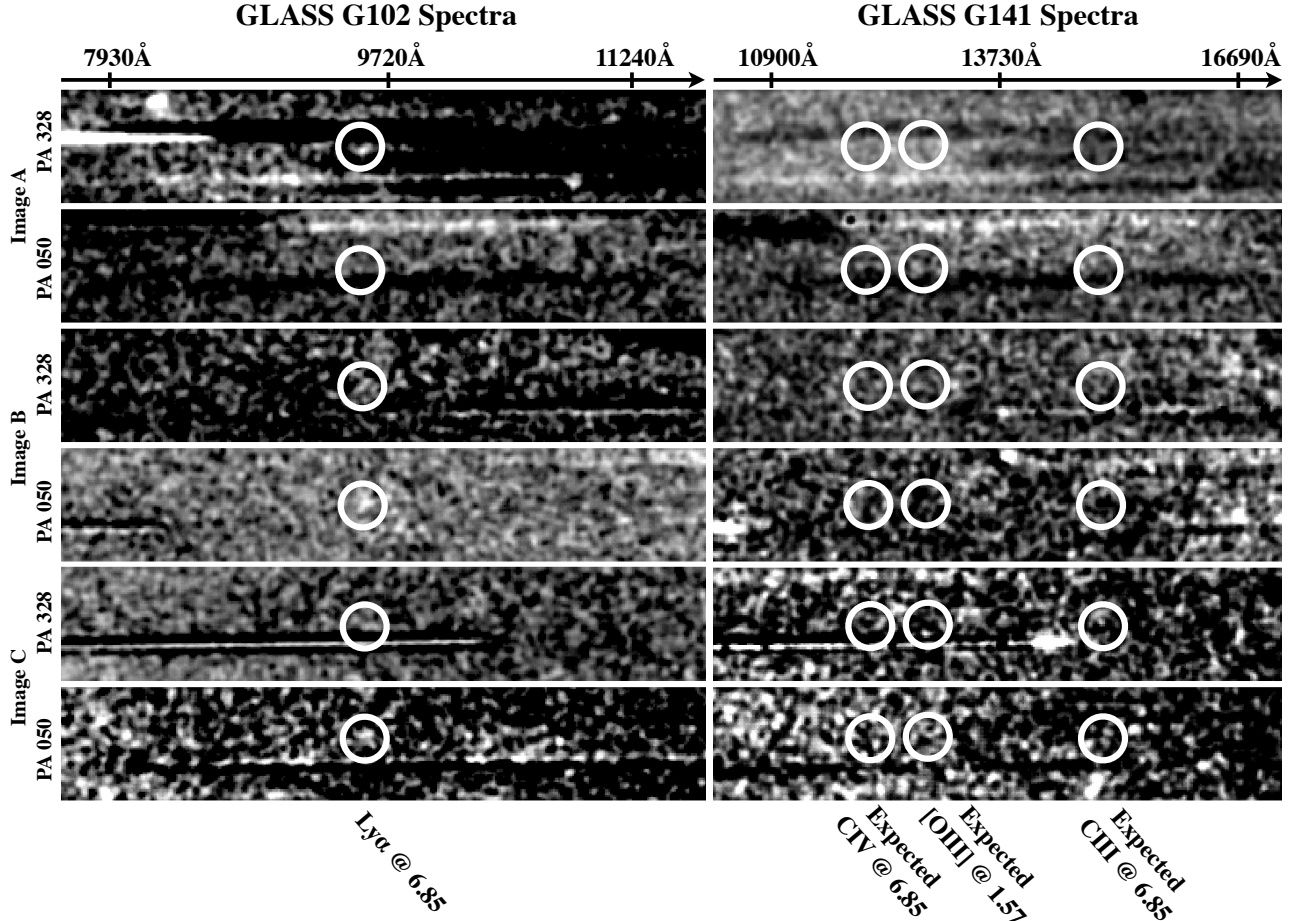
FIG. 3.— Contamination-subtracted *HST* G102 and G141 grism spectra for Images A, B, and C, obtained as part of the GLASS program. The grism data were taken at two different position angles (PAs; 50° and 328°), and we show each PA separately. The wavelengths of the *observed* Lyα and the *expected* C IV, and C III] lines at $z = 6.85$ are marked by white circles. We also mark the *expected* locations of the [O III] line at $z = 1.57$. We do not detect any significant flux at the expected wavelength of the potential [O III] line, and the upper limits on [O III]/[O II] strongly support the $z = 6.85$ Lyα interpretation.

2009), which constrains the gravitational potential of the cluster on a grid via an iterative χ^2 minimization algorithm. We find that our lens model is able to reproduce the positions and relative magnifications of the three images at $z = 6.85$, while also consistently fitting the other two systems used in the model. We therefore adopt the absolute magnifications of 11.0, 5.4, and 2.6 for Images A, B, and C, respectively.

5. DISCUSSION

We model the physical properties of the three images following the procedure outlined in Huang et al. (2016). In short, we adopt the Bruzual & Charlot (2003) (BC03) templates with $0.2 \, Z_\odot$ and a constant star formation history (SFH), motivated by the good recovery of SFRs and stellar masses of simulated galaxies (Salmon et al. 2015). We also account for dust attenuation internal to the galaxy following the prescription in Calzetti et al. (2000), parameterized by $E(B - V)_s$ from 0 to 1. The templates also include strong nebular emission lines, whose fluxes are determined by the Lyman continuum flux of BC03 models and nebular line ratios from Anders & Fritze-v. Alvensleben (2003). The fitting is done using the photometric redshift code EAZY (Brammer et al. 2008). In Figure 4 we show the best-fit $0.2 \, Z_\odot$ tem-

plates at the Lyα redshift $z_{\text{Lyα}} = 6.85$ and at the [O II] redshift $z_{\text{[OII]}} = 1.57$. In the bottom right panel, we also show the photometric redshift probability distribution $P(z)$ for each image. All three images have $P(z)$ more consistent with the Lyα redshift than with the [O II] redshift based on the total χ^2 values.

The modeling results are summarized in Table 1, where we report the best-fit values, 68% confidence intervals (and 84 percentile upper limits where they apply). After accounting for lens magnification, we find that this galaxy has rest-frame 1600Å absolute magnitude (converted from the observed F125W magnitudes) of -18.6 ± 0.2 mag, stellar mass of $(1.5 \pm 0.3) \times 10^7 \, M_\odot$, SFR of $1.4 \pm 0.2 \, M_\odot \, \text{yr}^{-1}$, and specific SFR (sSFR) of $95 \pm 25 \, \text{Gyr}^{-1}$ (all are S/N-weighted averages). The galaxy is also best fit by a very young ($\lesssim 20$ Myr old), dust-free template. The rest-frame UV slope β—measured from the median-stacked images—is $-2.76^{+1.23}_{-1.12}$, although the errors are large due to low S/N in the WFC3/IR filters. The results suggest that this galaxy is one of the intrinsically faintest Lyα-emitting galaxy confirmed at $z > 6$ to date; its rest-frame UV luminosity is roughly $0.14 \, L^*_{\text{UV}, \, z\sim7}$ (adopting $L^*_{\text{UV}, \, z\sim7} = -20.87 \pm 0.28$; Bouwens et al. 2015), well into
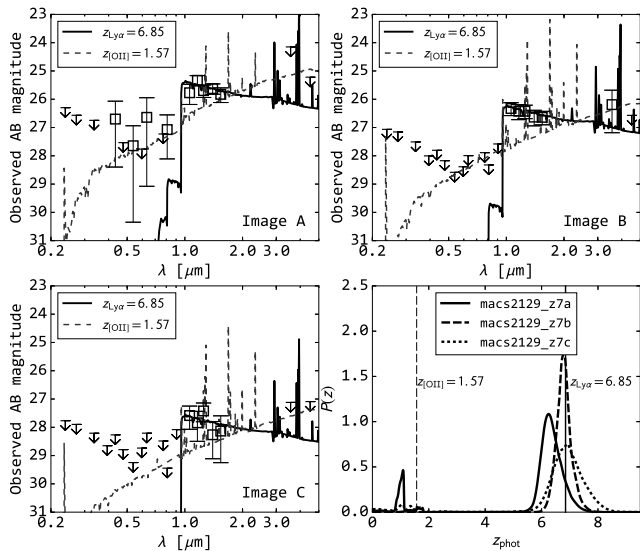
FIG. 4.— Best-fit 0.2 $Z_\odot$ SED templates for Images A, B, and C when the template redshift is fixed at $z_{\mathrm{Ly}\alpha} = 6.85$ (solid line) and at $z_{\mathrm{[OII]}} = 1.57$ (dashed line). Images A, B, and C are shown in the upper left, upper right, and bottom left panel, respectively. The photometric redshift probability distributions are shown in the lower right panel. All three images are better fit by a $z = 6.85$ template than a $z = 1.57$ template.

the faint end of the $z \sim 7$ UV LF. With the detection of Lyα emission from this galaxy (and from other similar galaxies), we start to probe the likely sources that dominated reionization: the low-mass, young, and (almost) dust-free galaxies (e.g., Robertson et al. 2015).

Recently, several galaxies at $z \gtrsim 7$ have been confirmed via their Lyα emission (e.g., Oesch et al. 2016, Song et al. 2016, and references therein). Most of these galaxies are surprisingly bright, with M_{UV} ranging from -20.5 to -22.4 mag; some of the aforementioned galaxies are selected based on their unusual *Spitzer*/IRAC colors, which imply very high [O III] or Hα EWs. Due to the depths of the available *Spitzer* imaging data, $z \gtrsim 7$ galaxies identified this way are mostly the bright ones (e.g., Roberts-Borsani et al. 2015). It is possible that these bright galaxies are sitting in overdense regions inside local HII bubbles that enhance Lyα transmission (Dijkstra 2014, and references therein) and offer a biased view of the reionization due to cosmic variance (Trenti & Stiavelli 2008). On the other hand, fainter galaxies hosted

by halos with mass $M \sim 10^{9-10}\ M_\odot$ are more likely to dominate the ionizing photon budget, the details of which will depend on a few factors like gas cooling, supernovae feedback, and ionizing photon escape fraction (e.g., Mesinger et al. 2016). So far all of the sub-L^* galaxies at $z \gtrsim 7$ confirmed via their Lyα emissions are detected behind galaxy clusters (see also Bradač et al. 2012 and Balestra et al. 2013); a larger sample of spectroscopically confirmed $z \gtrsim 7$ galaxy will be valuable for understanding the reionization process, e.g., through the Lyα fraction among LBGs (Pentericci et al. 2014).

In several ways, the galaxy probed here is similar to the $z = 6.4$ galaxy detected behind MACS0717+3745 (Vanzella et al. 2014). Both galaxies have faint UV luminosities ($\lesssim 0.2\ L^*$), low stellar masses ($\lesssim 5 \times 10^7\ M_\odot$), Ly$\alpha$ HWHM of ~ 100–150 km s^{-1}, and possibly high Lyα escape fractions ($\geq 10\%$). Perhaps the best local analogs of both galaxies are the Green Pea galaxies (e.g., Henry et al. 2015), which have high Lyα EWs (10–160Å), low stellar masses (10^8–$10^9\ M_\odot$), and blue UV slopes ($\beta \sim -2.2$ to -1.6) that suggest very low dust content. The detections of these sub-L^* galaxies at $z \gtrsim 7$ are made possible due to gravitational lensing, which will be the most efficient way to detect galaxies even in the *JWST* era.

REFERENCES

Anders, P., & Fritze-v. Alvensleben, U. 2003, A&A, 401, 1063
Balestra, I., Vanzella, E., Rosati, P., et al. 2013, A&A, 559, L9
Bouwens, R. J., Illingworth, G. D., Oesch, P. A., et al. 2015, ApJ, 803, 34
Bradač, M., Erben, T., Schneider, P., et al. 2005, A&A, 437, 49
Bradač, M., Treu, T., Applegate, D., et al. 2009, ApJ, 706, 1201
Bradač, M., Vanzella, E., Hall, N., et al. 2012, ApJ, 755, L7
Bradač, M., Ryan, R., Casertano, S., et al. 2014, ApJ, 785, 108
Bradley, L. D., Zitrin, A., Coe, D., et al. 2014, ApJ, 792, 76
Brammer, G. B., van Dokkum, P. G., & Coppi, P. 2008, ApJ, 686, 1503-1513
Bruzual, G., & Charlot, S. 2003, MNRAS, 344, 1000
Calzetti, D., Armus, L., Bohlin, R. C., et al. 2000, ApJ, 533, 682
Christensen, L., Richard, J., Hjorth, J., et al. 2012, MNRAS, 427, 1953
Coe, D., Bradley, L., & Zitrin, A. 2015, ApJ, 800, 84

Dijkstra, M. 2014, Publications of the Astron. Soc. of Australia, 31, e040
Ebeling, H., Barrett, E., Donovan, D., et al. 2007, ApJ, 661, L33
Erb, D. K., Pettini, M., Shapley, A. E., et al. 2010, ApJ, 719, 1168
Hayes, M., Östlin, G., Duval, F., et al. 2014, ApJ, 782, 6
Henry, A., Scarlata, C., Domínguez, A., et al. 2013, ApJ, 776, L27
Henry, A., Scarlata, C., Martin, C. L., & Erb, D. 2015, ApJ, 809, 19
Huang, K.-H., Bradač, M., Lemaux, B. C., et al. 2016, ApJ, 817, 11
Lemaux, B. C., Lubin, L. M., Sawicki, M., et al. 2009, ApJ, 700, 20
Merlin, E., Fontana, A., Ferguson, H. C., et al. 2015, A&A, 582, A15
Mesinger, A., Greig, B., & Sobacchi, E. 2016, arXiv:1602.07711
Monna, A., Seitz, S., Greisel, N., et al. 2014, MNRAS, 438, 1417

Oesch, P. A., Brammer, G., van Dokkum, P. G., et al. 2016, ApJ, 819, 129

Pentericci, L., Vanzella, E., Fontana, A., et al. 2014, ApJ, 793, 113

Postman, M., Coe, D., Benítez, N., et al. 2012, ApJS, 199, 25

Richard, J., Kneib, J.-P., Ebeling, H., et al. 2011, MNRAS, 414, L31

Rigby, J. R., Bayliss, M. B., Gladders, M. D., et al. 2015, ApJ, 814, L6

Robertson, B. E., Ellis, R. S., Furlanetto, S. R., & Dunlop, J. S. 2015, ApJ, 802, L19

Roberts-Borsani, G. W., Bouwens, R. J., Oesch, P. A., et al. 2015, arXiv:1506.00854

Salmon, B., Papovich, C., Finkelstein, S. L., et al. 2015, ApJ, 799, 183

Schaerer, D., de Barros, S., & Stark, D. P. 2011, A&A, 536, A72

Schmidt, K. B., Treu, T., Brammer, G. B., et al. 2014, ApJ, 782, L36

Schmidt, K. B., Treu, T., Bradač, M., et al. 2016, ApJ, 818, 38

Song, M., Finkelstein, S. L., Livermore, R. C., et al. 2016, arXiv:1602.02160

Stark, D. P., Richard, J., Siana, B., et al. 2014, MNRAS, 445, 3200

Stark, D. P., Richard, J., Charlot, S., et al. 2015, MNRAS, 450, 1846

Stark, D. P., Walth, G., Charlot, S., et al. 2015, MNRAS, 454, 1393

Trenti, M., & Stiavelli, M. 2008, ApJ, 676, 767-780

Treu, T., Schmidt, K. B., Brammer, G. B., et al. 2015, ApJ, 812, 114

Vanzella, E., Fontana, A., Zitrin, A., et al. 2014, ApJ, 783, L12

Zitrin, A., Zheng, W., Broadhurst, T., et al. 2014, ApJ, 793, L12

Zitrin, A., Fabris, A., Merten, J., et al. 2015, ApJ, 801, 44

Zitrin, A., Ellis, R. S., Belli, S., & Stark, D. P. 2015, ApJ, 805, L7